Atmos. Meas. Tech. Discuss., 8, 8257–8294, 2015
www.atmos-meas-tech-discuss.net/8/8257/2015/
doi:10.5194/amtd-8-8257-2015

Atmospheric Measurement Techniques Discussions

Observations of XCO_2 and XCH_4 with ground-based high-resolution FTS at Saga, Japan and comparisons with GOSAT products

H. Ohyama[1,a], S. Kawakami[1], T. Tanaka[1,b], I. Morino[2], O. Uchino[2], M. Inoue[2,c], T. Sakai[3], T. Nagai[3], A. Yamazaki[3], A. Uchiyama[3], T. Fukamachi[4], M. Sakashita[4], T. Kawasaki[4], T. Akaho[4], K. Arai[4], and H. Okumura[4]

[1]Japan Aerospace Exploration Agency, Tsukuba, Japan
[2]National Institute for Environmental Studies, Tsukuba, Japan
[3]Meteorological Research Institute, Tsukuba, Japan
[4]Graduate School of Science and Engineering, Saga University, Saga, Japan
[a]now at: Solar-Terrestrial Environment Laboratory, Nagoya University, Nagoya, Japan
[b]now at: NASA Ames Research Center, Moffett Field, CA 94035, USA
[c]now at: Department of Biological Environment, Akita Prefectural University, Akita, Japan

Received: 15 June 2015 – Accepted: 7 July 2015 – Published: 7 August 2015

Correspondence to: H. Ohyama (hohyama@stelab.nagoya-u.ac.jp)

Published by Copernicus Publications on behalf of the European Geosciences Union.

Abstract

Solar absorption spectra in the near-infrared region have been continuously acquired with a ground-based (g-b) high-resolution Fourier transform spectrometer (FTS) at Saga, Japan since July 2011. Column-averaged dry-air mole fractions of greenhouse gases were retrieved from the measured spectra for the period from July 2011 to December 2014. Aircraft measurements of CO_2 and CH_4 for calibrating the g-b FTS data were performed in January 2012 and 2013, and it is found that the g-b FTS and aircraft data agree to within ±0.2 %. The column-averaged dry-air mole fractions of CO_2 and CH_4 (XCO_2 and XCH_4) show increasing trends, with average growth rates of 2.3 ppm yr^{-1} and 9.5 ppb yr^{-1}, respectively, during the ∼ 3.5 yr of observation. We compared the g-b FTS XCO_2 and XCH_4 data with those derived from backscattered solar spectra in the short-wavelength infrared region measured with Thermal And Near-infrared Sensor for carbon Observation-Fourier Transform Spectrometer (TANSO-FTS) onboard the Greenhouse gases Observing SATellite (GOSAT). Average differences between TANSO-FTS and g-b FTS data (TANSO-FTS minus g-b FTS) are 0.40±2.51 ppm and −7.6 ± 13.7 ppb for XCO_2 and XCH_4, respectively. Using aerosol information measured with a sky radiometer at Saga, we found that the differences between the TANSO-FTS and g-b FTS data are moderately negatively correlated with aerosol optical thickness and do not depend explicitly on aerosol size. In addition, from aerosol profiles measured with lidar located right by the g-b FTS, we were able to show that cirrus clouds and tropospheric aerosols accumulated in the lower layers of the atmosphere tend to overestimate or underestimate the TANSO-FTS data.

1 Introduction

Atmospheric carbon dioxide (CO_2) and methane (CH_4) are major greenhouse gases, whose global annual mean concentrations have increased rapidly from 278 to 396 ppm for CO_2 and from 722 to 1824 ppb for CH_4 over the last 200 years (WMO, 2014). At

AMTD
8, 8257–8294, 2015

present, radiative forcing of atmospheric CO_2 and CH_4 accounts for approximately 65 and 17 % of the total radiative forcing by long-lived greenhouse gases, respectively (WMO, 2014). To accurately predict future atmospheric CO_2 and CH_4 concentrations and their impact on climate, it is necessary to understand how sources and sinks of CO_2 and CH_4 are distributed around the globe and how they change over time. Although the sources and sinks can be estimated from an inversion of surface air sample/in situ measurements, column abundances are also useful in constraining emissions (Yang et al., 2007; Keppel-Aleks et al., 2012) as well as sources and sinks (Chevallier et al., 2011) of CO_2. The Total Carbon Column Observing Network (TCCON) was established to derive column-averaged dry-air mole fractions of CO_2 and CH_4 (XCO_2 and XCH_4), in addition to several other trace gases (Wunch et al., 2011a).

Global XCO_2 and XCH_4 distributions are also derived from space-based instruments that are the Scanning Imaging Absorption Spectrometer for Atmospheric Chartography onboard Envisat (Bovensmann et al., 1999), the Thermal And Near-infrared Sensor for carbon Observation-Fourier Transform Spectrometer (TANSO-FTS) onboard the Greenhouse gases Observing SATellite (GOSAT) (Kuze et al., 2009), and the Orbiting Carbon Observatory-2 (XCO_2 only, Crisp et al., 2004; Boesch et al., 2011; Frankenberg et al., 2015). While satellite-based instruments can provide a global view, it is necessary to continuously validate these satellite products using data from instruments that have superior measurement precision and accuracy. Satellite data were validated using ground-based (g-b) high-resolution Fourier transform spectrometer (FTS) data obtained from TCCON (Cogan et al., 2012; Guerlet et al., 2013; Nguyen et al., 2014; Oshchepkov et al., 2012; Reuter et al., 2013; Yoshida et al., 2013) and aircraft profile CO_2 and CH_4 data collected with instruments installed on commercial airliners and chartered aircraft (Inoue et al., 2013, 2014). Guerlet et al. (2013), however, point out that additional validation sites with various atmospheric and land surface conditions are useful for improving retrieval algorithms.

We installed a high-resolution FTS instrument at Saga University (33.24° N, 130.29° E, 8 m a.s.l.), Japan in June 2011, and solar spectrum measurements have

AMTD
8, 8257–8294, 2015

been performed since the end of July 2011. This FTS is in operation under the TCCON requirements and to make a contribution to validating the satellite products. Air masses in the troposphere over Saga are dominated by transport from the Asian continent; however, depending on meteorological conditions, they may also be derived from the Pacific Ocean, especially in the summer season (Uchino et al., 2014). Because Saga and its surroundings are affected by continental aerosols and volcanic dust (Hidemori et al., 2014; Sakai et al., 2014), we have also been monitoring aerosols with a sky radiometer and a Mie lidar, which have been useful for evaluating the influence of aerosols on satellite retrievals. In the present study, we describe FTS instruments and analysis methods in Sects. 2 and 3, respectively, and present in Sect. 4 the calibration of the g-b FTS XCO_2 and XCH_4 values using aircraft measurements, time series of the g-b FTS data for the period of July 2011 to December 2014, short-term summer variations, and application of these data for validating TANSO-FTS products.

2 Instruments

2.1 Solar spectrum measurements

A FTS observation system was installed at Saga University, Japan in June 2011. Saga is located on the Tsukushi Plane, which covers an area of 1200 km^2, and is sandwiched between the Tsukushi Mountains in the north and the Ariake Sea in the south. Between 1981 and 2010, monthly mean precipitation amounts for June and July exceeded 300 mm (http://www.jma.go.jp/jma/indexe.html). The city consists of cultivated land and urban areas (http://www.biodic.go.jp/vg_map/vg_html/en/html/vg_map_frm_e.html).

Spectral measurements were taken with a Bruker IFS 125HR FTS instrument that has a maximum spectral resolution of 0.0035 cm^{-1} (defined as 0.9/maximum optical path difference). The FTS is housed in a recycled 12-foot shipping container located on the grounds of Saga University. The container is insulated and equipped with an air conditioning system to keep internal temperature and humidity stable. Sunlight is

AMTD
8, 8257–8294, 2015

directed into the container by a solar tracker (Bruker A547N), mounted on top of the container, and then introduced into the FTS by a folding mirror. The solar tracker is positioned inside a sliding dome to allow the tracker to move into every position, even in the closed state. The solar tracker features a quadrant photoelectric detector and a feedback system that enables the tracker to adjust the azimuth and elevation angles to keep solar radiation at a maximum. In order to protect the solar tracker from dust, we built a case made of polyvinyl chloride side surfaces and a top made of high-transmission glass (Asahi Glass, JFL5). In the spectral range above $\sim 5000\,cm^{-1}$, transmittance of the glass is approximately 90 %, and the wavenumber-dependence is small. Although the transmittance decreases from 90 % as the wavenumber becomes lower, spectra with a signal-to-noise ratio (SNR) of ~ 400 at $5000\,cm^{-1}$ can be obtained through the glass. The container has a precipitation sensor, allowing the sliding dome to close automatically when the sensor detects changes in conductivity due to rain and so on. An uninterruptible power supply is integrated to bridge power failures of up to two hours.

The FTS is equipped with two room temperature detectors, an indium gallium arsenide diode (InGaAs, 4000–12 000 cm^{-1}) and a silicon diode (Si, 9500–25 000 cm^{-1}). A spectral range from 3900 to 14 500 cm^{-1} can be measured simultaneously using a dual channel acquisition mode, with a $\sim 10\,000\,cm^{-1}$ cutoff dichroic filter (Optics Balzers). In addition to the room temperature detectors, liquid nitrogen cooled indium antimonide (InSb, 1850–10 000 cm^{-1}) and mercury cadmium telluride (MCT, 600–12 000 cm^{-1}) detectors are installed, although their data were not used in this study. The solar absorption spectra are acquired with a spectral resolution of $0.02\,cm^{-1}$, a scanner velocity of 7.5 kHz, and an aperture diameter of 1 mm. A calcium fluoride (CaF_2) beam splitter is used. Two scans, one forward and one backward, are individually carried out and recorded. One measurement for a single scan takes about 110 s. The pressure inside the FTS is kept at ~ 0.03 hPa with an oil-free scroll pump (Adixen, ACP15) to maintain stability of the system and to ensure clean and dry conditions.

AMTD
8, 8257–8294, 2015

2.2 Auxiliary data

A meteorological station, which consists of sensors for measuring surface pressure (Vaisala, PTB330), atmospheric temperature and relative humidity (Vaisala, HMP-155D), wind direction and speed (R. M. Young, 05103), rain amounts (Climatec, CTK-15PC), and solar and longwave radiation (Hukseflux, RA01), is installed next to the FTS container. Solar and longwave radiation are measured using a pyranometer and a pyrgeometer, respectively, which are part of a two-component radiation sensor. Data are recorded on a laptop computer with a frequency of 0.1 Hz through a data logger (Campbell, CR1000). Additionally, a sky radiometer, a Mie lidar, and an ozone differential absorption lidar are installed at Saga University for the purpose of validating the satellite data (Uchino et al., 2012a; Morino et al., 2013) and monitoring atmospheric aerosol and ozone.

2.3 Instrumental line shape (ILS) evaluation

For accurate retrievals of column abundance and/or column-averaged dry-air mole fractions, a good optical alignment of the FTS is crucial, and monitoring of the instrumental line shape (ILS) is important. The monitoring of the ILS is performed by spectral measurement of an HCl gas cell (length 10 cm, diameter 4 cm, filling pressure 5 mbar) located inside the FTS instrument and by spectral analysis using the LINEFIT 14.5 software (Hase et al., 1999, 2013). Figure 1a shows time series of the modulation efficiency amplitudes at the maximum optical pass difference (OPD), which represent a degree of the line width of the actual ILS compared to that of an ideal ILS. Figure 1b shows time series of the modulation efficiency phases averaged over the entire OPD, which indicate a measure for symmetry of the ILS. The average loss in modulation efficiency amplitude at maximum OPD is 3.0 ± 1.2 %, and we found that the ILS remained nearly constant during the ~ 3.5 yr of operation.

AMTD
8, 8257–8294, 2015

3 Analyses

3.1 Retrieval method

Atmospheric vertical column abundances of trace gases were derived from the measured interferograms using the GGG software package (version 20140418), which is used within TCCON as the common software package. Within GGG, first a solar absorption spectrum is created by performing a fast Fourier transform (FFT) of the interferogram, in which solar intensity variations caused by passing clouds and other disturbances are corrected (Keppel-Aleks et al., 2007). The spectrum is then analyzed using GFIT (version 4.4.10, a nonlinear least squares spectral fitting algorithm), in which an a priori profile is scaled to produce a synthetic spectrum that provides the best fit to the measured spectrum. Pressure, temperature, and water vapor profiles were obtained from National Centers for Environmental Prediction (NCEP) reanalysis data (Kalnay et al., 1996), and were interpolated in time and space to local solar noon and site geolocation, respectively. The tropospheric a priori CO_2 profile was created from an empirical model based on fits to GLOBALVIEW data, and the a priori profile above the tropopause decreases with altitude, depending on the age of the air (Andrews et al., 2001). The vertical spacing of the atmospheric parameters was set to 70 levels with a 1 km grid. From the solar absorption spectra obtained with the InGaAs detector, column abundances of CO_2, CH_4, CO, N_2O, H_2O, HDO, HF, and O_2 were derived. Figure 2a and b show examples of the spectral fits in the CO_2 and O_2 bands, respectively. Some large peaks of the residual (difference between the observed and the calculated spectra), especially in the CO_2 band, are due to discrepancies of solar lines.

The XCO_2 value was calculated as the ratio of CO_2 and dry-air column abundances. The dry-air column was derived from the O_2 column retrieved from the same spectra (i.e., O_2 column/0.2095). This procedure minimizes some systematic errors common to retrieved CO_2 and O_2 columns such as pressure errors, influence of the instrumental line shape, and tracker pointing errors (Wunch et al., 2011a). The column-averaged

AMTD
8, 8257–8294, 2015

dry-air mole fractions of the other species were calculated in a similar fashion. The air mass-dependent artifact found in the diurnal cycle, which was primarily caused by spectroscopic inadequacies, was corrected with an empirical derived equation described in Wunch et al. (2011a) and Deutscher et al. (2010) and was included in the GGG software package.

3.2 Screening method

In order to remove data of poor quality, we used the same screening criteria as described by Washenfelder et al. (2006), which is the standard for the TCCON dataset. Among them, FTS data affected by passing clouds were filtered using the fractional variation in solar intensity during a measurement. In our case, solar intensity variations (SIV) were measured by the pyranometer with a frequency of 0.1 Hz, and data with SIV of more than 5 % were screened out. However, the measurement frequency of the pyranometer may be not high enough to capture SIV occurring around the center burst of the interferogram, which significantly impacts the Fourier-transformed spectrum. We therefore set an additional criterion as follows. We calculated average values and their standard deviations (1σ) for $\sim$ 1000 data points at each side of the center burst of the interferogram. If the variability (1σ/average) of the interferogram was less than 5 % at both sides, the data were considered good quality.

When the solar zenith angle (SZA) becomes larger than 70°, the sunlight is disturbed by the connection between the glass and the polyvinyl chloride of the solar tracker protection case. At higher angles, although solar absorption spectra can be measured through the polyvinyl chloride, the SNR values of the spectra become worse. Therefore, data with SZAs larger than 70° were screened out. The data after applying these screening criteria are available at doi:10.14291/tccon.ggg2014.saga01.R0/1149283.

AMTD
8, 8257–8294, 2015

4 Results

4.1 Comparison with aircraft measurements

The g-b FTS data were corrected with TCCON common scale factors empirically determined using aircraft profiles over multiple TCCON sites to place the TCCON data on the World Meteorological Organization (WMO) standard reference scales (Wunch et al., 2010; Messerschmidt et al., 2011). We compared Saga FTS data with independent aircraft profiles to ensure that the TCCON common scale factors can be applied to the Saga FTS data. Several aircraft observation campaigns in Japan were performed for calibration of the g-b FTS measurements and validation of the GOSAT products (Tanaka et al., 2012). The aircraft measurements over Saga were performed using a Beechcraft King Air 200T on 9 and 13 January 2012 and 15 January 2013. The diameter of spiral flights was less than 10 km, and maximum altitudes were approximately 7 and 10 km for the 2012 and 2013 campaigns, respectively. Instrument settings used during the aircraft measurements are described in detail in Tanaka et al. (2012). During the aircraft campaigns in 2012, CO_2 profiles were measured in situ with a non-dispersive infrared gas analyzer (NDIR: LI-COR, LI-840) onboard the aircraft. In addition, flask sampling was performed at eight altitude levels to check accuracy of the in situ CO_2 profile and to obtain other trace gas concentrations such as CH_4, CO, N_2O, H_2, and SF_6. During the aircraft campaigns in 2013, in addition to the NDIR measurements and flask sampling, alternative CO_2 and CH_4 profiles were measured in situ with cavity ring-down spectroscopy (CRDS: picarro, G2301-m). For comparisons to the g-b FTS data, NDIR and flask data were used as aircraft profiles of CO_2 and CH_4 for 2012, respectively, while the CRDS data were used as the aircraft profiles for 2013. Note that the CO_2 profiles measured with NDIR and CRDS in 2013 are in agreement within ±0.2 ppm (Tanaka et al., 2015). Precision of the aircraft data is estimated to be 0.39 ppm and 4.5 ppb for the CO_2 and CH_4 mole fractions, respectively (Tanaka et al., 2015). Figure 3a and b show the measured CO_2 and CH_4 profiles for 15 January 2013, respectively. Additional vertical profiles of pressure, temperature, relative humidity, wind

AMTD
8, 8257–8294, 2015

direction, and wind speed were obtained by the Japan Weather Association under contract with the NIES using GPS radiosondes (Meisei Electric Co., RS-01G). Three temperature profiles measured on 15 January 2013 are shown in Fig. 3c.

Since the altitude ranges of the aircraft measurements were limited to approximately 0.5–7 or 0.5–10 km, the aircraft in situ profiles were extended below and above the flight altitude to cover the entire CO_2 and CH_4 profiles based on the assumption that the mole fractions in the boundary layer and the upper troposphere are constant against altitude. Aircraft in situ data were extrapolated to the surface using the lowest aircraft data. If aircraft measurements were not conducted up to the height of the tropopause, which was determined from the NCEP reanalysis data, the highest aircraft data were extended up to tropopause height. Above the highest aircraft height or the tropopause height, GFIT a priori profiles were attached to the aircraft data. Although the tropopause height can also be obtained from radiosonde temperature data measured during the aircraft observation campaign, the tropopause height determined from the NCEP reanalysis data was used in expanding the aircraft data to the stratosphere because it was used in creating the a priori profiles. The effect of the difference in tropopause height determination is evaluated below. Integrated CO_2 and CH_4 profiles are shown in Fig. 3a and b, respectively.

The XCO_2 values for the integrated aircraft profile were calculated according to the method of Wunch et al. (2010) for comparison with the retrieved $FTSXCO_2$:

$$\hat{c}_s = \gamma c_a + \left(\frac{VC^{aircraft}_{CO_2,ak} - \gamma VC^{a\ priori}_{CO_2,ak}}{VC_{air}} \right) \quad (1)$$

where c_a is the a priori XCO_2, γ is the retrieved scale factor, VC_{air} is the vertical column of dry-air, and $VC^{aircraft}_{CO_2,ak}$ and $VC^{a\ priori}_{CO_2,ak}$ are vertical columns of CO_2 form aircraft and a priori profiles, respectively, with a column averaging kernel applied. The effect of the column averaging kernel of FTS was taken into account to equalize the sensitivities of the CO_2 mole fraction at each altitude for the total column. Since FTS data aver-

AMTD
8, 8257–8294, 2015

aged over a time window of ±3 h relative to the time of the aircraft measurements are compared to the aircraft data, column averaging kernels averaged over the same time window were used for the calculation. In addition, the column averaging kernels are the average of the used retrieval windows. Table 1 lists the integrated aircraft and average FTS XCO_2 values. The differences in XCO_2 between FTS and aircraft measurements are within ±0.21 %. The differences in XCH_4 between the two measurements are within ± 0.22 % (Table 2). Tables 1 and 2 include results obtained using tropopause heights determined from radiosonde temperature profiles. The differences in tropopause height introduce differences of up to 0.11 % in estimating aircraft XCO_2 and XCH_4 values. Nevertheless, since uncertainties (2σ) in the TCCON common scale factor are approximately 0.2 and 0.4 % for XCO_2 and XCH_4, respectively (Wunch et al., 2010), we find that the Saga FTS fall within this range of uncertainties and can be calibrated to the WMO standard reference scales.

4.2 Time series

Figure 4a–c shows time series of XCO_2, XCH_4, and XCO values observed at Saga during the period from July 2011 to December 2014. Both seasonal and interannual variations can be seen. We determined the seasonal and trend components in the time series using a fitting procedure described by Thoning et al. (1989), which is based on a low-pass filtering technique using FFT. Series of harmonic functions with 12- and 6-months periods were employed to represent seasonal variations, and low-pass filters with a 2 year cutoff frequency for the long-term trend and a 150 day cutoff frequency for the short-term trend were used. The summation of the harmonic functions and the two filtered datasets is treated as the fitting curve of XCO_2. For XCH_4 and XCO, the summation of the harmonic functions and the long-term trend is regarded as the fitting curve. The fitting curves and the long-term trends of the retrieved values are shown in Fig. 4. Standard deviations of the differences between the retrieved values and the fitting curves are 0.81 ppm, 12.1 ppb, and 13.3 ppb for XCO_2, XCH_4, and XCO, respectively.

AMTD
8, 8257–8294, 2015

The peak-to-peak seasonal amplitude of XCO_2 was 6.9 ppm over Saga during July 2011 and December 2014, with a seasonal maximum and minimum in the average seasonal cycle during May and September, respectively. The long-term trend of the retrieved XCO_2 shows a monotonic increase. The growth rate of XCO_2, which is a derivative of the long-term trend over time, is almost constant, and we obtained an average growth rate of 2.3 ppm yr^{-1} for XCO_2, similar to the global mean growth rate based on sampling measurements (WMO, 2014). The XCH_4 time series is characterized by large variability of XCH_4 during the summer season, which is discussed in the next section, as well as an increasing trend with an average growth rate of 9.5 ppb yr^{-1}. The XCO time series has features of a seasonal cycle along with multiple peaks and a moderately decreasing trend with a growth rate of -1.0 ppb yr^{-1}.

4.3 Source of short-term variations

During the summer season, relatively low XCO_2 values, approximately 3–4 ppm lower than the fitting curve, were observed. As for XCH_4, the observed XCO_2 values in the summer season indicate a larger variability compared to the other seasons. In order to investigate the causes of this variation, backward trajectory calculations were performed with the NCEP Global Data Assimilation System data using the Hybrid Single-Particle Lagrangian Integrated Trajectory (HYSPLIT) model (Draxler and Rolph, 2013). Ten-day isentropic backward trajectories were started at 2.6 km altitude (approximately 700 hPa) above the Saga FTS site. This height was selected because the change in potential temperature at 700 hPa correlates with the XCO_2 variation (Keppel-Aleks et al., 2012). Figure 5a and b shows the results of the backward trajectories for days of year (DOY) 1–90 (January to March; winter season) and 170–260 (mid-June to mid-September; summer season), respectively. The trajectories for the summer season were classified into three types, depending on of air mass transport. If the start point of the trajectory was located north of 35° N and west of 145° E, the trajectories were classified as type I. If the start point of the trajectory was located south of 35° N and west of 120° E, the trajectories were classified as type II. If the start point was located

AMTD
8, 8257–8294, 2015

anywhere else, the trajectories were classified as type III. However, provided that an air mass was located for a longer period of time west of 130° E, the trajectories were classified as type II. The trajectories for types I, II, and III relate to transport of air masses from the Asian continent (China), Southeast Asia, and the Pacific Ocean, respectively, and are colored in green (China), red (Southeast Asia), and blue (Pacific) in Fig. 5b. For the remaining days (April to mid-June and mid-September to December) not shown in Fig. 5, the transport from the Asian continent is dominant. Then, in order to derive short-term variations of XCO_2, XCH_4, and XCO, the respective long-term trends and seasonal cycles were subtracted from the observed values, and the residual values are referred to as ΔXCO_2, ΔXCH_4, and ΔXCO. Figure 6a and b show correlation plots of $\Delta XCO/\Delta XCO_2$ and $\Delta XCH_4/\Delta XCO$, respectively, whose values are represented by the daily mean values.

Figures 5b and 6a show that most of the low-XCO_2 events in the summer season are driven by long-range transport of air masses associated with strong biospheric uptake over the Asian continent. Wada et al. (2007) reported that low-CO_2 events at ground level in the summer season were observed at Minamitorishima Island (24.3° N, 154.0° E) in the Northwest Pacific. We note that the air masses passing over Saga are expected to travel toward Minamitorishima Island. With regard to XCO, high-XCO events correspond to transport of air masses from the Asian continent or Southeast Asia, while low-XCO events correspond to air mass transport from the Pacific Ocean. As a whole, the $\Delta XCO/\Delta XCO_2$ ratio for the summer season is anti-correlated with a correlation coefficient of −0.47. For the winter season, the correlation coefficient is 0.62, and it is probable that the burning of fossil fuel causes the positive steep slope of the $\Delta XCO/\Delta XCO_2$ ratio.

As shown in Fig. 6b, the slope of the $\Delta XCH_4/\Delta XCO$ ratio for the summer season is steeper than that for the winter season. The most likely cause for the steep slope of the $\Delta XCH_4/\Delta XCO$ ratio is the transport of air masses from Southeast Asia and/or the southern part of China where CH_4 emissions from rice fields significantly increase during the summer (Bergamaschi et al., 2009). In addition, transport of air masses

AMTD
8, 8257–8294, 2015

from the Pacific Ocean, where CH_4 concentrations are low, may contribute to the steep slope of the $\Delta XCH_4/\Delta XCO$ ratio during the summer. Although the ΔXCO values remain high during the winter, the decrease in CH_4 emissions over Asia during the winter causes the gentle slope of the $\Delta XCH_4/\Delta XCO$ ratio for the winter season. The correlation coefficients are 0.91 and 0.61 for the summer and winter data, respectively.

The $\Delta XCO/\Delta XCO_2$, $\Delta XCO/\Delta XCH_4$, and $\Delta XCH_4/\Delta XCO_2$ ratios at Saga over the period from 2011 to 2014 were compared with $\Delta CO/\Delta CO_2$, $\Delta CO/\Delta CH_4$, and $\Delta CH_4/\Delta CO_2$ ratios at Hateruma Island, Japan (24.05° N, 123.80° E) that were derived from in situ observation over the period from 1999 to 2010 (Tohjima et al., 2014). Since the temporal and spatial distributions of CO_2, CH_4, and CO are attributed mainly to their emissions and following transports, the ratios among CO_2, CH_4, and CO derived from column observation are comparable to those derived from in situ observation (Wong et al., 2015). The $\Delta XCO/\Delta XCO_2$, $\Delta XCO/\Delta XCH_4$, and $\Delta XCH_4/\Delta XCO_2$ ratios for the summer season ($-5.94\,\mathrm{ppb\,ppm^{-1}}$, $0.70\,\mathrm{ppb\,ppb^{-1}}$, and $-9.40\,\mathrm{ppb\,ppm^{-1}}$) are comparable with the $\Delta CO/\Delta CO_2$, $\Delta CO/\Delta CH_4$, and $\Delta CH_4/\Delta CO_2$ ratios for the summer season in Tohjima et al. (2014), while the $\Delta XCO/\Delta XCO_2$, $\Delta XCO/\Delta XCH_4$, and $\Delta XCH_4/\Delta XCO_2$ ratios for the winter season ($16.6\,\mathrm{ppb\,ppm^{-1}}$, $1.19\,\mathrm{ppb\,ppb^{-1}}$, and $7.33\,\mathrm{ppb\,ppm^{-1}}$) are significantly smaller than Tohjima et al. (2014). Assuming that their emissions for the winter season have similar spatial distribution over East Asian, the comparison results imply that the emissions over the period from 2012 to 2014 relatively decrease in the order corresponding to CO, CH_4, and CO_2 or increase in the order corresponding to CO_2, CH_4, and CO, compared to before 2010. However, since $\Delta XCO_2/\Delta XCO$ ratios in China, which have been derived from satellite XCO_2 and XCO observations, differ depending on megacity (Silva et al., 2013), the differences in observed ratios at Saga and Hateruma Island might reflect the differences in regional emissions from East Asia. In order to separate the temporal and spatial contributions to the differences in observed ratios, the continuous observational data and top-down approach with high spatial resolution (e.g., Turner et al., 2015) are required.

AMTD
8, 8257–8294, 2015

4.4 Validation of TANSO-FTS SWIR products

As described in the previous section, except for transport from the Pacific Ocean during the summer season, air masses over Saga are derived from the Asian continent, where large aerosol optical depth is observed (van Donkelaar et al., 2010). From observations of aerosols at Fukue Island (~ 150 km west–southwest of Saga), the transport of continental aerosols is indicated (Hidemori et al., 2014). Therefore, the Saga g-b FTS data are believed to be appropriate for validation of the XCO_2 and XCH_4 retrievals from the satellite-borne short-wavelength infrared (SWIR) spectra in moderately aerosol-loaded scenes. We compared the g-b FTS XCO_2 and XCH_4 data with those derived from the SWIR spectra measured with TANSO-FTS onboard GOSAT. The TANSO-FTS XCO_2 and XCH_4 products used here are general public user subsets of version 02.21 (before 24 May 2014) and version 02.31 (after 16 June 2014). Figure 7a and b shows a time series of XCO_2 and XCH_4 from the g-b FTS and TANSO-FTS measurements. The TANSO-FTS data are selected within a ±2.0° latitude/longitude rectangular area centered on the FTS site, while the complete g-b FTS data are presented in those figures. The TANSO-FTS can observe seasonal variations of XCO_2 and XCH_4 similar to the g-b FTS, but the TANSO-FTS data show a higher degree of scattering than the g-b FTS data.

In order to accurately compare physical quantities obtained from two kinds of remote sensing instruments, it is necessary to consider the effects of differences in a priori profile and vertical resolution (i.e., column averaging kernel). First, to conform to a common a priori profile, the TANSO-FTS data were adjusted to the TCCON a priori profile (Wunch et al., 2011b). The average difference between the adjusted and the raw TANSO-FTS XCO_2 data (adjusted minus raw data) is −0.02 ppm with a standard deviation of 0.17 ppm. The average difference for XCH_4 data is -4.34 ± 0.84 ppb. Secondly, the TCCON data were smoothed by the TANSO-FTS column averaging kernel to simulate what the TANSO-FTS would observe, provided that the TCCON data were true. The average difference between the smoothed and the raw TCCON XCO_2 data

AMTD
8, 8257–8294, 2015

(smoothed minus raw data) is −0.08 ppm with a standard deviation of 0.12 ppm. The average difference for the XCH_4 data is 0.02±0.18 ppb. We then compared the TANSO-FTS data adjusted to the TCCON a priori profile with the TCCON data smoothed by the TANSO-FTS column averaging kernel.

A correlation plot for TANSO-FTS and g-b FTS XCO_2 values is shown in Fig. 8a, and a correlation plot for XCH_4 is shown in Fig. 8b. If the g-b FTS data were collected within ±30 min of the GOSAT overpass time (around 13:25 LT), the average data and corresponding TANSO-FTS data are plotted. Therefore, the number of TANSO-FTS data in the correlation plots (Fig. 8) is less than that in the time series (Fig. 7). The average difference between TANSO-FTS XCO_2 values and g-b FTS data is 0.40 ± 2.51 ppm (average difference ± standard deviation). As for XCH_4, the TANSO-FTS data are biased low by 7.6 ppb with a standard deviation of 13.7 ppb, compared to the g-b FTS data. The correlation coefficients amount to 0.74 and 0.68 for XCO_2 and XCH_4, respectively. The average differences between TANSO-FTS and g-b FTS data are within the range of validation results using other TCCON site data (Yoshida et al., 2013), but with slightly larger standard deviations.

Figure 9a and b illustrates the differences between TANSO-FTS and g-b FTS values for XCO_2 and XCH_4 as a function of the aerosol optical thickness (AOT) values at 870 nm, which were observed with the sky radiometer (Kobayashi et al., 2006) located at Saga. We note that the AOT is here defined as the aerosol optical depth (AOD) of an entire atmosphere (Bohren and Clothiaux, 2006). The match-up was limited to a ±1.0° latitude/longitude rectangular area to highlight the local effect of aerosols on the differences between TANSO-FTS and g-b FTS data. The sky radiometer data were selected in the same manner as the g-b FTS data (i.e., average of data within ±30 min of the GOSAT overpass time). The correlation coefficients of the difference between TANSO-FTS and g-b FTS data and the AOT values are −0.25 and −0.07 for XCO_2 and XCH_4, respectively. The differences between TANSO-FTS and g-b FTS data are independent of the Ångström exponent, which is a measure of the size of the aerosol particles.

AMTD
8, 8257–8294, 2015

Next, the effects of aerosol and cirrus profiles on the TANSO-FTS XCO_2 and XCH_4 retrievals were investigated. Figure 10a and b shows vertical profiles of the backscattering ratio (R) and total depolarization ratio at 532 nm (Dep.), and of the backscatter-related wavelength exponent between 532 and 1064 nm (Alp), which were measured with lidar at Saga (Uchino et al., 2012b). Aerosols on 29 May 2012 in Fig. 10a were uniformly distributed below a height of 3 km and the AOD for 0–10 km was large (i.e., 1.28, assuming an aerosol extinction-to-backscatter ratio of 50 sr). In this case, the differences between TANSO-FTS and g-b FTS data are −4.82 ppm for XCO_2 and −7.2 ppb for XCH_4. On 8 November 2013 shown in Fig. 10b, thin cirrus clouds was observed around 8.5 km and the AOD was 0.018 assuming an aerosol extinction-to-backscatter ratio of 20 sr. Total AOD, including aerosols below 2 km was 0.49 for the altitude range of 0–15 km. The XCO_2 and XCH_4 differences are positively biased, namely 4.01 ppm and 19.5 ppb, respectively. For two other cases of cirrus clouds (not shown), we found a positive bias of XCO_2. Therefore, a treatment of cirrus clouds in the TANSO-FTS XCO_2 and XCH_4 retrievals will be incorporated in the next version of the Level 2 algorithm (Y. Yoshida, personal communication, 2015). As a whole, effects of aerosols on the TANSO-FTS retrievals result in a weak negative correlation of the differences between TANSO-FTS and g-b FTS data against AOT as well as in a large scatter of TANSO-FTS data.

5 Conclusions

Near-infrared solar absorption spectra between 3900 and 14 500 cm^{-1} have been measured with a g-b FTS, installed at Saga, Japan. We have retrieved column-averaged dry-air mole fractions of CO_2, CH_4, and several other gas species from the solar absorption spectra, using the TCCON standard retrieval algorithm. From HCl gas cell measurements and analyses, we find that the ILS of the FTS is stable during its ~ 3.5 yr operation. The XCO_2 and XCH_4 values derived from the g-b FTS measurements were compared with those derived from aircraft measurements. The differences between g-b

AMTD
8, 8257–8294, 2015

FTS and aircraft data are within ±0.21 and ±0.22 % for XCO_2 and XCH_4, respectively. A curve fitting procedure applied to a July 2011 to December 2014 time series of g-b FTS data, showed that the retrieved XCO_2 values had an average seasonal amplitude of 6.9 ppm and a growth rate of 2.3 ppm yr^{-1}. The XCH_4 values indicate an increasing trend with a growth rate of 9.5 ppb yr^{-1}, while the XCO values showed a decreasing trend with a growth rate of −1.0 ppb yr^{-1}. Based on the relationship between the deviations from the fitting curve (ΔXCO_2, ΔXCH_4, and ΔXCO) and the back trajectory patterns, we found that the variations of XCO_2, XCH_4, and XCO over Saga during the summer season can be ascribed to the transport of air masses affected by biospheric activities over the Asian continent or transport of air masses from the Pacific Ocean. The steep slope of $\Delta XCO/\Delta XCO_2$ for the winter season is suggestive of air masses influenced by fossil fuel combustion. The XCO_2 and XCH_4 values derived from the g-b FTS measurements were compared with those derived from the TANSO-FTS measurements. The average difference in XCO_2 between the TANSO-FTS and g-b FTS data is 0.40 ppm with a standard deviation of 2.51 ppm. The average difference for XCH_4 is -7.6 ± 13.7 ppb. It is found that the differences in XCO_2 and XCH_4 show a moderate negative correlation with the AOT and are independent of aerosol size. From the aerosol profiles, which were measured simultaneously with lidar at Saga, we find that TANSO-FTS data tend to be overestimated or underestimated when cirrus clouds and tropospheric aerosols with large optical depth are present.

Acknowledgements. We are grateful to T. Machida of the NIES for his assistance with the aircraft measurements. We also thank C. Taura of the Saga University for operation of the g-b FTS. Part of this research was supported by the Environment Research and Technology Development Fund (2A-1102) of the Ministry of the Environment, Japan. The authors gratefully acknowledge the NOAA Air Resources Laboratory (ARL) for the provision of the HYSPLIT transport and dispersion model and READY website (http://www.ready.noaa.gov) used in this publication.

AMTD
8, 8257–8294, 2015

References

Andrews, A., Boering, K., Daube, B., Wofsy, S., Loewenstein, M., Jost, H., Podolske, J., Webster, C., Herman, R., Scott, D., Flesch, G. J., Moyer, E. J., Elkins, J. W., Dutton, G. S., Hurst, D. F., Moore, F. L., Ray, E. A., Romashkin, P. A., and Strahan, S. E.: Mean ages of stratospheric air derived from in situ observations of CO_2, CH_4, and N_2O, J. Geophys. Res., 106, 32295–32314, doi:10.1029/2001JD000465, 2001.

Bergamaschi, P., Frankenberg, C., Meirink, J. F., Krol, M., Villani, M. G., Houweling, S., Dentener, F., Dlugokencky, E. J., Miller, J. B., Gatti, L. V., Engel, A., and Levin, I.: Inverse modeling of global and regional CH_4 emissions using SCIAMACHY satellite retrievals, J. Geophys. Res., 114, D22301, doi:10.1029/2009JD012287, 2009.

Boesch, H., Backer, D., Connor, B., Crips, D., and Miller, C.: Global characterization of CO_2 column retrievals from shortwave-infrared satellite observations of the Orbiting Carbon Observatory-2 mission, Remote Sens., 3, 270–304, doi:10.3390/rs3020270, 2011.

Bohren, C. F. and Clothiaux, E. E.: Fundamentals of Atmospheric Radiation: an Introduction with 400 Problems, Wiley-VCH, New York, 2006.

Bovensmann, H., Burrows, J. P., Buchwitz, M., Frerick, J., Noël, S., Rozanov, V. V., Chance, K. V., and Goede, A.: SCIAMACHY – mission objectives and measurement modes, J. Atmos. Sci., 56, 127–150, doi:10.1175/1520-0469(1999)056<0127:SMOAMM>2.0.CO;2, 1999.

Cogan, A. J., Boesch, H., Parker, R. J., Feng, L., Palmer, P. I., Blavier, J.-F. L., Deutscher, N. M., Macatangay, R., Notholt, J., Roehl, C., Warneke, T., and Wunch, D.: Atmospheric carbon dioxide retrieved from the Greenhouse gases Observing SATellite (GOSAT): comparison with ground-based TCCON observations and GEOS-Chem model calculations, J. Geophys. Res., 117, D21301, doi:10.1029/2012JD018087, 2012.

Crisp, D., Atlas, R. M., Breon, F.-M., Brown, L. R., Burrows, J. P., Ciais, P., Connor, B. J., Doney, S. C., Fung, I. Y., Jacob, D. J., Miller, C. E., O'Brien, D., Pawson, S., Randerson, J. T., Rayner, P., Salawitch, R. J., Sander, S. P., Sen, B., Stephens, G. L., Tans, P. P., Toon, G. C., Wennberg, P. O., Wofsy, S. C., Yung, Y. L., Kuang, Z., Chudasama, B., Sprague, G., Weiss, B., Pollock, R., Kenyon, D., and Schroll, S.: The Orbiting Carbon Observatory (OCO) mission, Adv. Space Res., 34, 700–709, doi:10.1016/j.asr.2003.08.062, 2004.

Deutscher, N. M., Griffith, D. W. T., Bryant, G. W., Wennberg, P. O., Toon, G. C., Washenfelder, R. A., Keppel-Aleks, G., Wunch, D., Yavin, Y., Allen, N. T., Blavier, J.-F., Jiménez, R.,

AMTD
8, 8257–8294, 2015

Daube, B. C., Bright, A. V., Matross, D. M., Wofsy, S. C., and Park, S.: Total column CO_2 measurements at Darwin, Australia – site description and calibration against in situ aircraft profiles, Atmos. Meas. Tech., 3, 947–958, doi:10.5194/amt-3-947-2010, 2010.

Draxler, R. R. and Rolph, G. D.: HYSPLIT (HYbrid Single-Particle Lagrangian Integrated Trajectory) Model access via NOAA ARL READY Website, available at: http://www.arl.noaa.gov/HYSPLIT.php (last access: 15 May 2015), NOAA Air Resources Laboratory, College Park, MD, 2013.

Frankenberg, C., Pollock, R., Lee, R. A. M., Rosenberg, R., Blavier, J.-F., Crisp, D., O'Dell, C. W., Osterman, G. B., Roehl, C., Wennberg, P. O., and Wunch, D.: The Orbiting Carbon Observatory (OCO-2): spectrometer performance evaluation using pre-launch direct sun measurements, Atmos. Meas. Tech., 8, 301–313, doi:10.5194/amt-8-301-2015, 2015.

Guerlet, S., Butz, A., Schepers, D., Basu, S., Hasekamp, O. P., Kuze, A., Yokota, T., Blavier, J.-F., Deutscher, N. M., Griffith, D. W., Hase, F., Kyro, E., Morino, I., Sherlock, V., Sussmann, R., Galli, A., and Aben, I.: Impact of aerosol and thin cirrus on retrieving and validating XCO_2 from GOSAT shortwave infrared measurements, J. Geophys. Res., 118, 4887–4905, doi:10.1002/jgrd.50332, 2013.

Hase, F., Blumenstock, T., and Paton-Walsh, C.: Analysis of the instrumental line shape of high resolution Fourier transform IR spectrometers with gas cell measurements and new retrieval software, Appl. Optics, 38, 3417–3422, doi:10.1364/AO.38.003417, 1999.

Hase, F., Drouin, B. J., Roehl, C. M., Toon, G. C., Wennberg, P. O., Wunch, D., Blumenstock, T., Desmet, F., Feist, D. G., Heikkinen, P., De Mazière, M., Rettinger, M., Robinson, J., Schneider, M., Sherlock, V., Sussmann, R., Té, Y., Warneke, T., and Weinzierl, C.: Calibration of sealed HCl cells used for TCCON instrumental line shape monitoring, Atmos. Meas. Tech., 6, 3527–3537, doi:10.5194/amt-6-3527-2013, 2013.

Hidemori, T., Nakayama, T., Matsumi, Y., Kinugawa, T., Yabushita, A., Ohashi, M., Miyoshi, T., Irei, S., Takami, A., Kaneyasu, N., Yoshino, A., Suzuki, R., Yumoto, Y., and Hatakeyama, S.: Characteristics of atmospheric aerosols containing heavy metals measured on Fukue Island, Japan, Atmos. Environ., 97, 447–455, doi:10.1016/j.atmosenv.2014.05.008, 2014.

Inoue, M., Morino, I., Uchino, O., Miyamoto, Y., Yoshida, Y., Yokota, T., Machida, T., Sawa, Y., Matsueda, H., Sweeney, C., Tans, P. P., Andrews, A. E., Biraud, S. C., Tanaka, T., Kawakami, S., and Patra, P. K.: Validation of XCO_2 derived from SWIR spectra of GOSAT TANSO-FTS with aircraft measurement data, Atmos. Chem. Phys., 13, 9771–9788, doi:10.5194/acp-13-9771-2013, 2013.

AMTD
8, 8257–8294, 2015

Inoue, M., Morino, I., Uchino, O., Miyamoto, Y., Saeki, T., Yoshida, Y., Yokota, T., Sweeney, C., Tans, P. P., Biraud, S. C., Machida, T., Pittman, J. V., Kort, E. A., Tanaka, T., Kawakami, S., Sawa, Y., Tsuboi, K., and Matsueda, H.: Validation of XCH_4 derived from SWIR spectra of GOSAT TANSO-FTS with aircraft measurement data, Atmos. Meas. Tech., 7, 2987–3005, doi:10.5194/amt-7-2987-2014, 2014.

Kalnay, E., Kanamitsu, M., Kistler, R., Collins, W., Deaven, D., Gandin, L., Iredell, M., Saha, S., White, G., Woollen, J., Zhu, Y., Leetmaa, A., Reynolds, B., Chelliah, M., Ebisuzaki, W., Higgins, W., Janowiak, J., Mo, K. C., Ropelewski, C., Wang, J., Jenne, R., and Joseph, D.: The NCEP/NCAR 40-year reanalysis project, B. Am. Meteorol. Soc., 77, 437–471, doi:10.1175/1520-0477(1996)077<0437:TNYRP>2.0.CO;2, 1996.

Keppel-Aleks, G., Toon, G. C., Wennberg, P. O., and Deutscher, N. M.: Reducing the impact of source brightness fluctuations on spectra obtained by Fourier-transform spectrometry, Appl. Optics, 46, 4774–4779, doi:10.1364/AO.46.004774, 2007.

Keppel-Aleks, G., Wennberg, P. O., Washenfelder, R. A., Wunch, D., Schneider, T., Toon, G. C., Andres, R. J., Blavier, J.-F., Connor, B., Davis, K. J., Desai, A. R., Messerschmidt, J., Notholt, J., Roehl, C. M., Sherlock, V., Stephens, B. B., Vay, S. A., and Wofsy, S. C.: The imprint of surface fluxes and transport on variations in total column carbon dioxide, Biogeosciences, 9, 875–891, doi:10.5194/bg-9-875-2012, 2012.

Kobayashi, E., Uchiyama, A., Yamazaki, A., and Matsuse, K.: Application of the maximum likelihood method to the inversion algorithm for analyzing aerosol optical properties from sun and sky radiance measurements, J. Meteorol. Soc. Jpn., 84, 1047–1062, 2006.

Kuze. A., Suto. H., Nakajima, M., and Hamazaki, T.: Thermal and near infrared sensor for carbon observation Fourier transform spectrometer on the Greenhouse Gases Observing Satellite for greenhouse gases monitoring, Appl. Optics, 48, 6716–6733, doi:10.1364/AO.48.006716, 2009.

Machida, T., Matsueda, H., Sawa, Y., Nakagawa, Y., Hirotani, K., Kondo, N., Goto, K., Nakazawa, T., Ishikawa, K., and Ogawa, T.: Worldwide measurements of atmospheric CO_2 and other trace gas species using commercial airlines, J. Atmos. Ocean. Tech., 25, 1744–1754, doi:10.1175/2008JTECHA1082.1, 2008.

Messerschmidt, J., Geibel, M. C., Blumenstock, T., Chen, H., Deutscher, N. M., Engel, A., Feist, D. G., Gerbig, C., Gisi, M., Hase, F., Katrynski, K., Kolle, O., Lavrič, J. V., Notholt, J., Palm, M., Ramonet, M., Rettinger, M., Schmidt, M., Sussmann, R., Toon, G. C., Truong, F., Warneke, T., Wennberg, P. O., Wunch, D., and Xueref-Remy, I.: Calibration of TCCON

AMTD
8, 8257–8294, 2015

column-averaged CO_2: the first aircraft campaign over European TCCON sites, Atmos. Chem. Phys., 11, 10765–10777, doi:10.5194/acp-11-10765-2011, 2011.

Morino, I., Sakai, T., Nagai, T., Uchiyama, A., Yamazaki, A., Kawakami, S., Ohyama, H., Arai, K., Okumura, H., Shibata, T., Nagahama, T., Kikuchi, N., Yoshida, Y., Liley, B., Sherlock, V., Robinson, J., Uchino, O., Yokota, T.: Impact of aerosols and cirrus clouds on the GOSAT-observed CO_2 and CH_4 inferred from ground-based lidar, skyradiometer and FTS data at prioritized observation sites, AGU Fall Meeting, San Francisco, 9–13 December 2013, Abstract A21G-0152, 2013.

Nguyen, H., Osterman, G., Wunch, D., O'Dell, C., Mandrake, L., Wennberg, P., Fisher, B., and Castano, R.: A method for colocating satellite XCO_2 data to ground-based data and its application to ACOS-GOSAT and TCCON, Atmos. Meas. Tech., 7, 2631–2644, doi:10.5194/amt-7-2631-2014, 2014.

Oshchepkov, S., Bril, A., Yokota, T., Morino, I., Yoshida, Y., Matsunaga, T., Belikov, D., Wunch, D., Wennberg, P. O., Toon, G. C., O'Dell, C. W., Butz, A., Guerlet, S., Cogan, A., Boesch, H., Eguchi, N., Deutscher, N. M., Griffith, D., Macatangay, R., Notholt, J., Sussmann, R., Rettinger, M., Sherlock, V., Robinson, J., Kyrö, E., Heikkinen, P., Feist, D. G., Nagahama, T., Kadygrov, N., Maksyutov, S., Uchino, O., and Watanabe, H.: Effects of atmospheric light scattering on spectroscopic observations of greenhouse gases from space: validation of PPDF-based CO_2 retrievals from GOSAT, J. Geophys. Res., 117, 1–18, doi:10.1002/jgrd.50146, 2012.

Reuter, M., Bovensmann, H., Buchwitz, M., Burrows, J. P., Connor, B. J., Deutscher, N. M., Griffith, D. W. T., Heymann, J., Keppel-Aleks, G., Messerschmidt, J., Notholt, J., Petri, C., Robinson, J., Schneising, O., Sherlock, V., Velazco, V., Warneke, T., Wennberg, P. O., and Wunch, D.: Retrieval of atmospheric CO_2 with enhanced accuracy and precision from SCIAMACHY: validation with FTS measurements and comparison with model results, J. Geophys. Res., 116, D04301, doi:10.1029/2010JD015047, 2011.

Rodgers, C. D.: Inverse Methods For Atmospheric Sounding: Theory and Practice, vol. 2 of Series on Atmospheric, Oceanic and Planetary Physics, World Scientific, River Edge, NJ, 2000.

Rodgers, C. D. and Connor, B. J.: Intercomparison of remote sounding instruments, J. Geophys. Res., 108, 4116, doi:10.1029/2002JD002299, 2003.

AMTD
8, 8257–8294, 2015

Rolph, G. D.: Real-Time Environmental Applications and Display sYstem (READY), available at: http://www.ready.noaa.gov (last access: 15 May 2015), NOAA Air Resources Laboratory, College Park, MD, 2013.

Sakai, T., Uchino, O., Morino, I., Nagai, T., Akaho, T., Kawasaki, T., Okumura, H., Arai, K., Uchiyama, A., Yamazaki, A., Matsunaga, T., and Yokota, T.: Vertical distribution and optical properties of volcanic ash from Mt. Sakurajima detected with lidar and skyradiometer over Saga (in Japanese with English abstract), J. Remote Sens. Soc. Japan, 34, 197–204, doi:10.11440/rssj.34.197, 2014.

Silva, S. J., Arellano, A. F., and Worden, H.: Toward anthropogenic combustion emission constraints from space-based analysis of urban CO_2/CO sensitivity, Geophys. Res. Lett., 40, 4971–4976, doi:10.1002/grl.50954, 2013.

Tanaka, T., Miyamoto, Y., Morino, I., Machida, T., Nagahama, T., Sawa, Y., Matsueda, H., Wunch, D., Kawakami, S., and Uchino, O.: Aircraft measurements of carbon dioxide and methane for the calibration of ground-based high-resolution Fourier Transform Spectrometers and a comparison to GOSAT data measured over Tsukuba and Moshiri, Atmos. Meas. Tech., 5, 2003–2012, doi:10.5194/amt-5-2003-2012, 2012.

Tanaka, T., Yates, E., Iraci, L., Johnson, M. S., Gore, W., Tadić, J. M., Loewenstein, M., Kuze, A., Frankenberg, C., Butz, A., and Yoshida, Y.: Two year comparison of airborne measurements of CO_2 and CH_4 with GOSAT at Railroad Valley, Nevada, IEEE T. Geosci. Remote Sens., in review, 2015.

Thoning, K. W., Tans, P. P., and Komhyr, W. D.: Atmospheric carbon dioxide at Mauna Loa Observatory 2. Analysis of the NOAA GMCC data, 1974–1985, J. Geophys. Res., 94, 8549–8565, doi:10.1029/JD094iD06p08549, 1989.

Tohjima, Y., Kubo, M., Minejima, C., Mukai, H., Tanimoto, H., Ganshin, A., Maksyutov, S., Katsumata, K., Machida, T., and Kita, K.: Temporal changes in the emissions of CH_4 and CO from China estimated from CH_4/CO_2 and CO/CO_2 correlations observed at Hateruma Island, Atmos. Chem. Phys., 14, 1663–1677, doi:10.5194/acp-14-1663-2014, 2014.

Turner, A. J., Jacob, D. J., Wecht, K. J., Maasakkers, J. D., Lundgren, E., Andrews, A. E., Biraud, S. C., Boesch, H., Bowman, K. W., Deutscher, N. M., Dubey, M. K., Griffith, D. W. T., Hase, F., Kuze, A., Notholt, J., Ohyama, H., Parker, R., Payne, V. H., Sussmann, R., Sweeney, C., Velazco, V. A., Warneke, T., Wennberg, P. O., and Wunch, D.: Estimating global and North American methane emissions with high spatial resolution using GOSAT satellite data, Atmos. Chem. Phys., 15, 7049–7069, doi:10.5194/acp-15-7049-2015, 2015.

AMTD
8, 8257–8294, 2015

Uchino, O., Kikuchi, N., Sakai, T., Morino, I., Yoshida, Y., Nagai, T., Shimizu, A., Shibata, T., Yamazaki, A., Uchiyama, A., Kikuchi, N., Oshchepkov, S., Bril, A., and Yokota, T.: Influence of aerosols and thin cirrus clouds on the GOSAT-observed CO_2: a case study over Tsukuba, Atmos. Chem. Phys., 12, 3393–3404, doi:10.5194/acp-12-3393-2012, 2012a.

Uchino, O., Sakai, T., Nagai, T., Nakamae, K., Morino, I., Arai, K., Okumura, H., Takubo, S., Kawasaki, T., Mano, Y., Matsunaga, T., and Yokota, T.: On recent (2008–2012) stratospheric aerosols observed by lidar over Japan, Atmos. Chem. Phys., 12, 11975–11984, doi:10.5194/acp-12-11975-2012, 2012b.

van Donkelaar, A., Martin, R. V., Brauer, M., Kahn, R., Levy, R., Verduzco, C., and Villeneuve, P. J.: Global estimates of ambient fine particulate matter concentrations from satellite-based aerosol optical depth: development and application, Environ. Health Persp., 118, 847–855, doi:10.1289/ehp.0901623, 2010.

Wada, A., Sawa, Y., Matsueda, H., Taguchi, S., Murayama, S., Okubo, S., and Tsutsumi, Y.: Influence of continental air mass transport on atmospheric CO_2 in the western North Pacific, J. Geophys. Res., 112, D07311, doi:10.1029/2006JD007552, 2007.

Washenfelder, R. A., Toon, G. C., Blavier, J.-F., Yang, Z., Allen, N. T., Wennberg, P. O., Vay, S. A., Matross, D. M., and Daube, B. C.: Carbon dioxide column abundances at the Wisconsin Tall Tower site, J. Geophys. Res., 111, D22305, doi:10.1029/2006JD007154, 2006.

Wong, K. W., Fu, D., Pongetti, T. J., Newman, S., Kort, E. A., Duren, R., Hsu, Y.-K., Miller, C. E., Yung, Y. L., and Sander, S. P.: Mapping CH_4 : CO_2 ratios in Los Angeles with CLARS-FTS from Mount Wilson, California, Atmos. Chem. Phys., 15, 241–252, doi:10.5194/acp-15-241-2015, 2015.

World Meteorological Organization: The State of Greenhouse Gases in the Atmosphere Based on Global Observations Through 2013, WMO Greenhouse Gas Bulletin, 10, Geneva, 2014.

Wunch, D., Toon, G. C., Wennberg, P. O., Wofsy, S. C., Stephens, B. B., Fischer, M. L., Uchino, O., Abshire, J. B., Bernath, P., Biraud, S. C., Blavier, J.-F. L., Boone, C., Bowman, K. P., Browell, E. V., Campos, T., Connor, B. J., Daube, B. C., Deutscher, N. M., Diao, M., Elkins, J. W., Gerbig, C., Gottlieb, E., Griffith, D. W. T., Hurst, D. F., Jiménez, R., Keppel-Aleks, G., Kort, E. A., Macatangay, R., Machida, T., Matsueda, H., Moore, F., Morino, I., Park, S., Robinson, J., Roehl, C. M., Sawa, Y., Sherlock, V., Sweeney, C., Tanaka, T., and Zondlo, M. A.: Calibration of the Total Carbon Column Observing Network using aircraft profile data, Atmos. Meas. Tech., 3, 1351–1362, doi:10.5194/amt-3-1351-2010, 2010.

AMTD
8, 8257–8294, 2015

Wunch, D., Toon, G. C., Blavier, J.-F. L., Washenfelder, R. A., Notholt, J., Connor, B. J., Griffith, D. W. T., Sherlock, V., and Wennberg, P. O.: The Total Carbon Column Observing Network, Philos. T. R. Soc. A, 369, 2087–2112, doi:10.1098/rsta.2010.0240, 2011a.

Wunch, D., Wennberg, P. O., Toon, G. C., Connor, B. J., Fisher, B., Osterman, G. B., Frankenberg, C., Mandrake, L., O'Dell, C., Ahonen, P., Biraud, S. C., Castano, R., Cressie, N., Crisp, D., Deutscher, N. M., Eldering, A., Fisher, M. L., Griffith, D. W. T., Gunson, M., Heikkinen, P., Keppel-Aleks, G., Kyrö, E., Lindenmaier, R., Macatangay, R., Mendonca, J., Messerschmidt, J., Miller, C. E., Morino, I., Notholt, J., Oyafuso, F. A., Rettinger, M., Robinson, J., Roehl, C. M., Salawitch, R. J., Sherlock, V., Strong, K., Sussmann, R., Tanaka, T., Thompson, D. R., Uchino, O., Warneke, T., and Wofsy, S. C.: A method for evaluating bias in global measurements of CO_2 total columns from space, Atmos. Chem. Phys., 11, 12317–12337, doi:10.5194/acp-11-12317-2011, 2011b.

Yang, Z., Washenfelder, R., Keppel-Aleks, G., Krakauer, N., Randerson, J., Tans, P., Sweeney, C., and Wennberg, P.: New constraints on Northern Hemisphere growing season net flux, Geophys. Res. Lett., 34, L12807, doi:10.1029/2007GL029742, 2007.

Yoshida, Y., Kikuchi, N., Morino, I., Uchino, O., Oshchepkov, S., Bril, A., Saeki, T., Schutgens, N., Toon, G. C., Wunch, D., Roehl, C. M., Wennberg, P. O., Griffith, D. W. T., Deutscher, N. M., Warneke, T., Notholt, J., Robinson, J., Sherlock, V., Connor, B., Rettinger, M., Sussmann, R., Ahonen, P., Heikkinen, P., Kyrö, E., Mendonca, J., Strong, K., Hase, F., Dohe, S., and Yokota, T.: Improvement of the retrieval algorithm for GOSAT SWIR XCO_2 and XCH_4 and their validation using TCCON data, Atmos. Meas. Tech., 6, 1533–1547, doi:10.5194/amt-6-1533-2013, 2013.

AMTD
8, 8257–8294, 2015

Table 1. Comparison between XCO_2 values derived from g-b FTS and aircraft measurement. The values in the second, fourth, and fifth columns represent the results obtained using tropopause heights determined from NCEP reanalysis data and radiosonde temperature profiles (in brackets) over Saga. Aircraft data are weighted by the column averaging kernel of the g-b FTS.

Date	Tropopause height [km]	FTS [ppm]	Aircraft [ppm]	(FTS–Aircraft)/ Aircraft [%]
9 Jan 2012	14.425 (14.333)	395.60	395.04 (395.04)	0.14 (0.14)
13 Jan 2012	15.521 (14.967)	395.17	394.51 (394.49)	0.17 (0.17)
15 Jan 2013	15.945 (8.667)	397.24	396.39 (396.72)	0.21 (0.13)

AMTD
8, 8257–8294, 2015

Table 2. Same as Table 1, but for XCH_4 values.

Date	Tropopause height [km]	FTS [ppm]	Aircraft [ppm]	(FTS–Aircraft)/ Aircraft [%]
9 Jan 2012	14.425 (14.333)	1.827	1.823 (1.823)	0.22 (0.22)
13 Jan 2012	15.521 (14.967)	1.825	1.828 (1.827)	–0.16 (–0.11)
15 Jan 2013	15.945 (8.667)	1.836	1.838 (1.840)	–0.11 (–0.22)

AMTD
8, 8257–8294, 2015

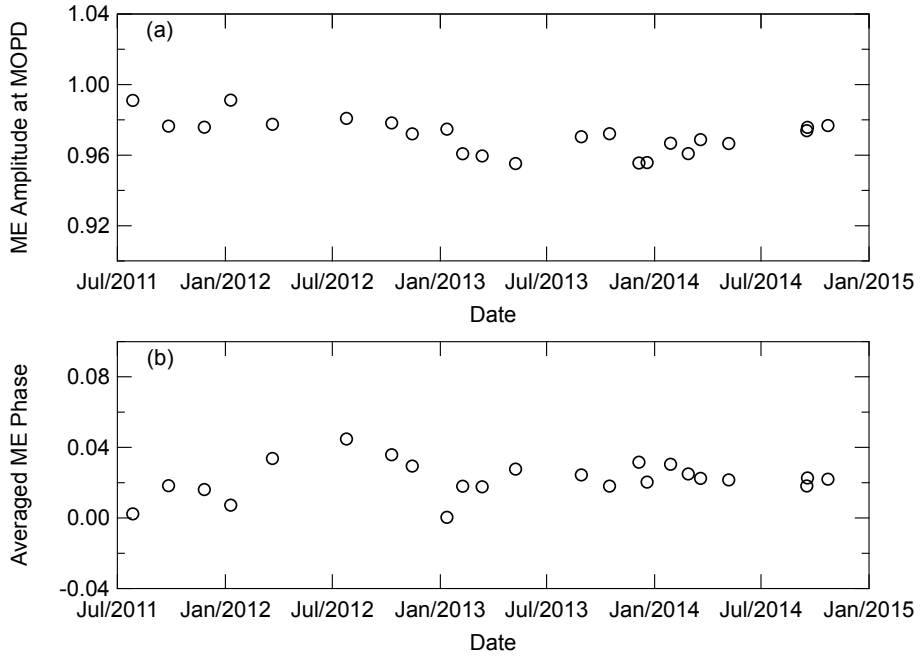

Figure 1. (a) Modulation efficiency amplitude at the maximum optical pass difference (OPD) and **(b)** modulation efficiency phase averaged over the whole OPD, which are evaluated from HCl cell spectra using the LINEFIT 14.5 software.

AMTD
8, 8257–8294, 2015

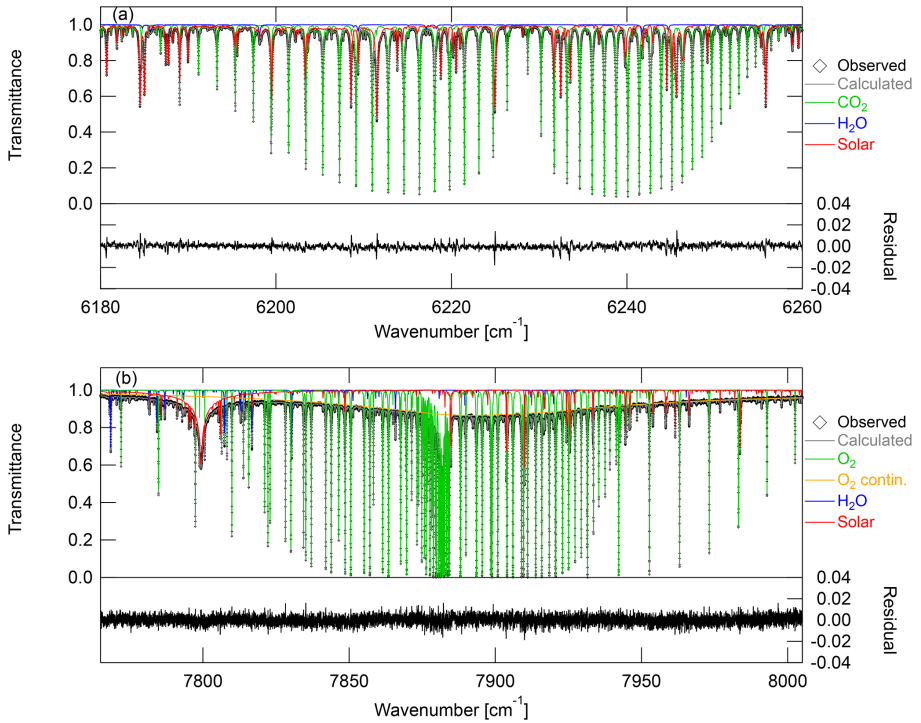

Figure 2. Examples of spectral fits for **(a)** CO_2 and **(b)** O_2 bands. Black diamonds denote the observed spectra on 26 November 2011, and colored lines denote the calculated spectra for the telluric and solar lines. Residuals between the observed and calculated spectra are also shown.

AMTD
8, 8257–8294, 2015

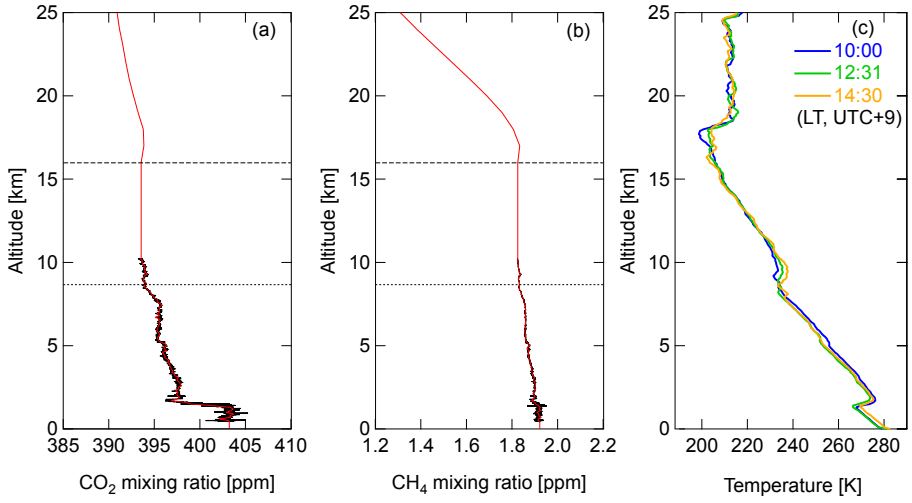

Figure 3. In situ **(a)** CO_2 and **(b)** CH_4 profiles measured by instruments onboard aircraft over the Saga FTS site on 15 January 2013. Black line represents the measured data, red line is the integrated profile (see text); dashed and dotted lines indicate tropopause height determined from NCEP reanalysis data and radiosonde temperature profiles, respectively. **(c)** Temperature profiles measured by radiosonde launched from Saga on 15 January 2013.

AMTD
8, 8257–8294, 2015

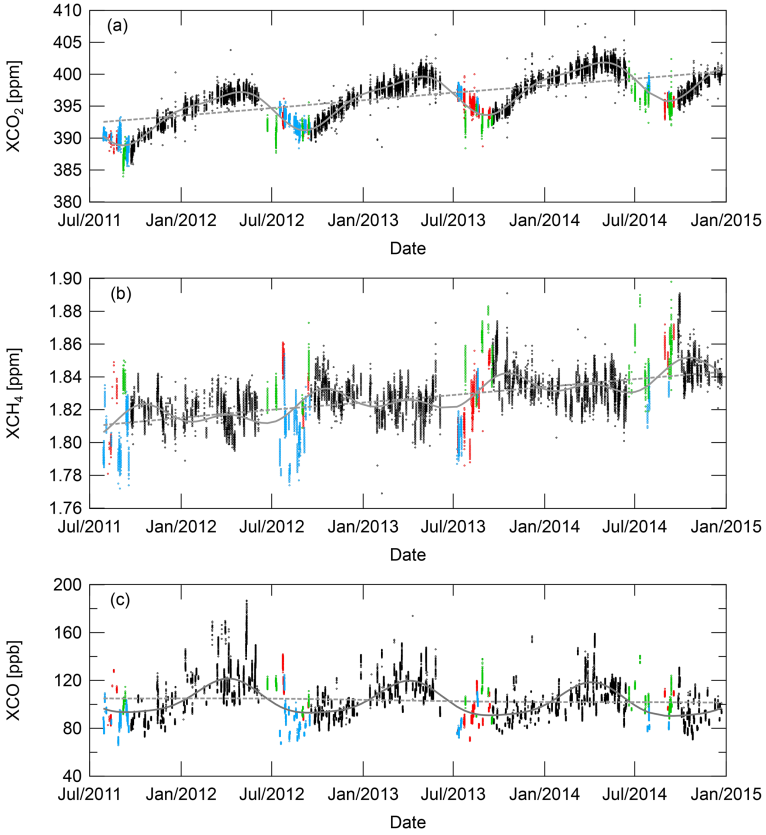

Figure 4. Time series of **(a)** XCO_2, **(b)** XCH_4, and **(c)** XCO values at Saga for the period of July 2011 to December 2014. Colors correspond to those of the trajectories for DOY 170–260 shown in Fig. 5b. Fitting curves (grey solid lines) and long-term trends (grey dashed lines) are also shown.

AMTD
8, 8257–8294, 2015

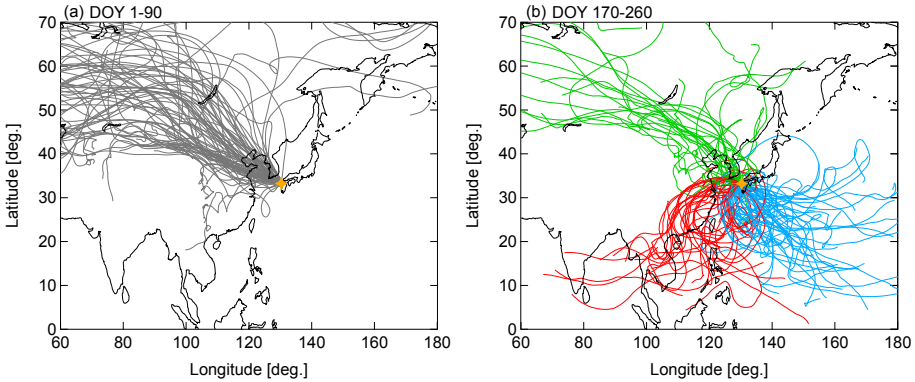

Figure 5. Ten-day isentropic backward trajectories from Saga at 03:00 UT on **(a)** DOY 1–90 and **(b)** DOY 170–260. The trajectories are started from an altitude of 2.6 km (approximately 700 hPa). The trajectories of DOY 170–260 are classified into three types, depending on of air mass transport, and the classification approach is described in the text.

AMTD
8, 8257–8294, 2015

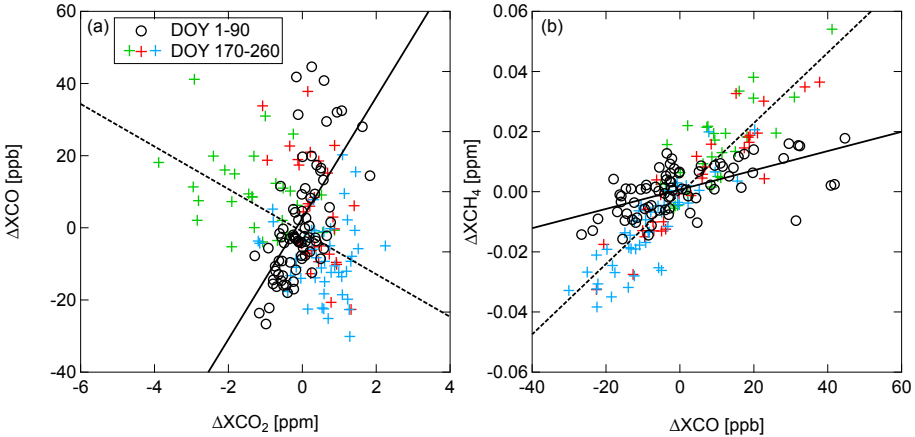

Figure 6. Correlation plots of **(a)** ΔXCO and ΔXCO_2 and **(b)** ΔXCH_4 and ΔXCO, which are represented by the differences between g-b FTS data and fitting curve values. Black circles are data for DOY 1–90; colored crosses are data for DOY 170–260. Colors correspond to those of the trajectories shown in Fig. 5b. Solid and dashed lines denote linear fits to DOY 1–90 and DOY 170–260 data, respectively.

AMTD
8, 8257–8294, 2015

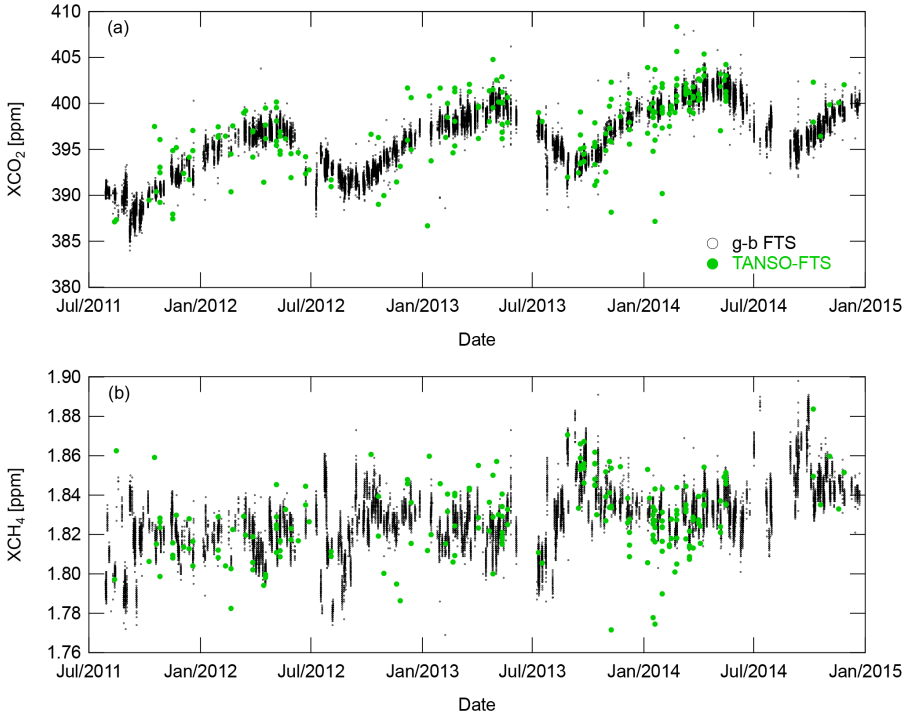

Figure 7. Time series of **(a)** XCO_2 and **(b)** XCH_4 for g-b FTS and TANSO-FTS data. Black circles are the g-b FTS data; green circles are the TANSO-FTS data within a ±2.0° latitude/longitude rectangular area centered on the FTS site.

AMTD
8, 8257–8294, 2015

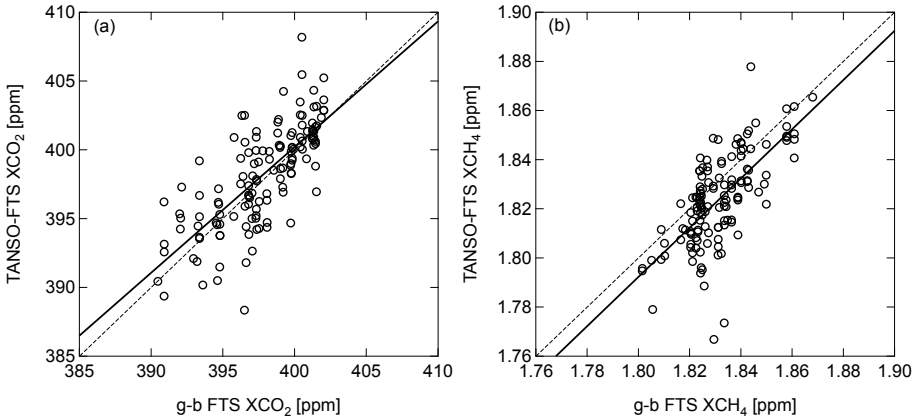

Figure 8. Correlation plots of **(a)** XCO_2 and **(b)** XCH_4 values derived from the g-b FTS and the TANSO-FTS spectra. The g-b FTS data within ±30 min of the GOSAT overpass time are averaged. Solid and dashed lines denote linear fit with an intercept of zero and one-to-one line, respectively.

AMTD
8, 8257–8294, 2015

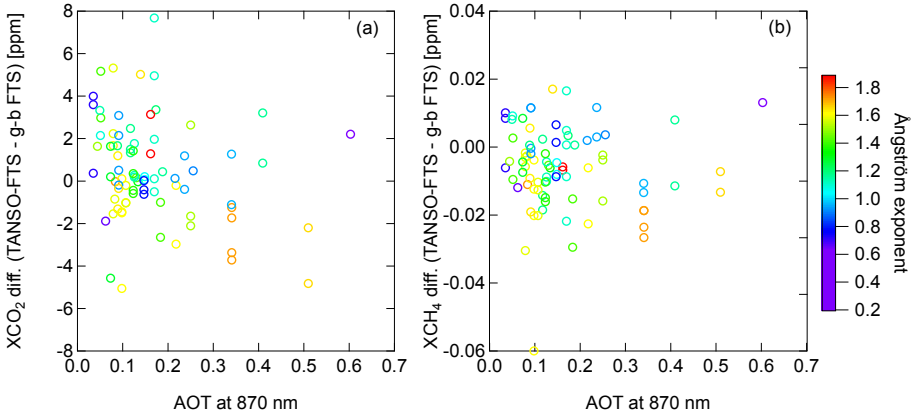

Figure 9. (a) Differences between XCO_2 values derived from TANSO-FTS and g-b FTS spectra with respect to aerosol optical thickness at 870 nm measured with the sky radiometer at Saga. Color scale represents Ångström exponent derived from the sky radiometer measurements. **(b)** Same as Fig. 9a, but for XCH_4 values.

AMTD
8, 8257–8294, 2015

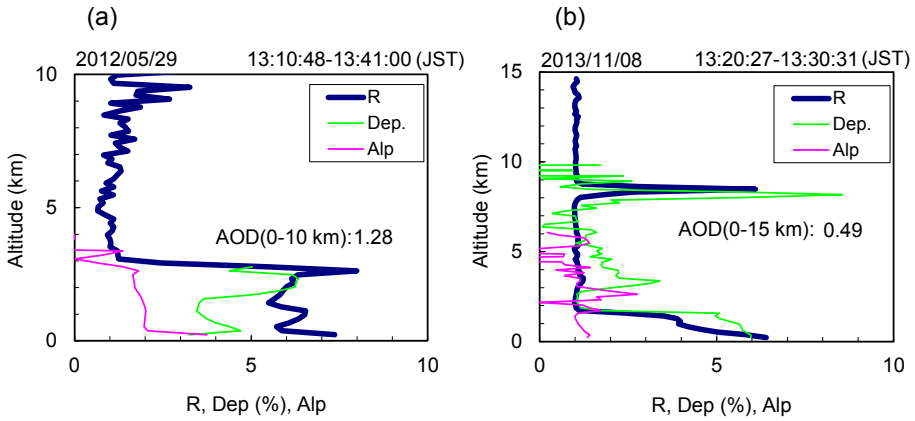

Figure 10. Vertical profiles of the backscattering ratio (cobalt), total depolarization ratio (green), and backscatter-related wavelength exponent (pink), measured with the Mie lidar at Saga on **(a)** 29 May 2012 and **(b)** 8 November 2013.

AMTD
8, 8257–8294, 2015